International Journal of Power Electronics and Drive System (IJPEDS)
Vol. 17, No. 3, September 2026, pp. 1885~1901
ISSN: 2088-8694, DOI: 10.11591/ijpeds.v17.i3.pp1885-1901 ❒ 1885

Analytical design, modelling and simulation of an LLC resonant converter for an electric vehicle auxiliary power module

Mohamad Affan Mohd Noh[1], Jacques Juicy Patureau Ravina[1], Sivakumar Sivanesan[1], Hafizul Azizi Ismail[1], Ali Akbar Firoozi[2]
[1]School of Engineering, Asia Pacific University of Technology and Innovation, Kuala Lumpur, Malaysia
[2]Faculty of Engineering & Technology, University of Botswana, Gaborone, Botswana

Article Info

Article history:

Received Aug 13, 2025
Revised Feb 10, 2026
Accepted Jul 8, 2026

Keywords:

Analytical design
Auxiliary power module
LLC resonant converter
Simulation model
Transformer

ABSTRACT

This paper presents an analytical design, modelling, and simulation of an LLC resonant converter for an electric vehicle auxiliary power module (APM). The work contributes a complete LLC-focused workflow that starts from design specifications and proceeds through: i) Resonant-tank selection using normalized gain–frequency maps to choose the inductance ratio L_n and a quality factor Q_e with soft-switching in mind; ii) Transformer sizing from core data and loss limits; and iii) Small-signal-based PI controller tuning those accounts for the plant's inherent inversion. The workflow is implemented and validated in MATLAB Simulink and PLECS for input voltages of 235-265 V and load levels from 10% to 100%. The converter achieves a peak efficiency of 98.1% within an 80.6-128.3 kHz switching range, full-load efficiency of 93.5%, and about ±1% output voltage regulation. The controller maintains stable output settling times of 0.42-0.44 ms during 100% to 80% load steps and the reverse transition. At the highest input voltage, the switching frequency drifts beyond the intended range, which indicates a clear target for controller refinement in future work. The results show that the proposed analytical workflow is practical for designing LLC converters that meet APM efficiency and regulation goals, with cross-platform simulation providing consistent evidence of performance.

Corresponding Author:

Mohamad Affan Mohd Noh
School of Engineering, Asia Pacific University of Technology and Innovation
Kuala Lumpur 57000, Malaysia
Email: mohamad.affan@apu.edu.my

1. INTRODUCTION

The automotive industry is rapidly transitioning towards electrification, evidenced by a significant increase in global electric vehicle (EV) sales over the past decade, transforming the transportation landscape [1]. This shift is primarily driven by the need to address climate change and reduce greenhouse gas (GHG) emissions, prompting extensive research into the electrification of transportation [2]. The electrification of transportation in the transportation sector is driven by the need for sustainable, energy-efficient, and environmentally friendly solutions to replace conventional internal combustion engine vehicles. The replacement of conventional internal combustion engine vehicles with electrification has heightened the role of auxiliary power modules (APMs) in electric vehicles (EVs). APMs supply low-voltage power to critical subsystems such as infotainment, lighting, and climate control, drawing energy from the high-voltage traction battery. Because APMs must operate over wide input-voltage ranges, meet stringent efficiency requirements, and maintain low electromagnetic interference (EMI), robust design methodologies are essential to achieving stable, compact, and high-performance isolated DC–DC conversion [1]-[6].

Conventional isolated topologies such as phase-shifted full bridge (PSFB), asymmetrical half bridge (AHB), and SIMO-based converters provide functional power conversion but often lack design-level transparency: soft-switching boundaries, magnetic constraints, and control interactions are not inherently coupled to a unified analytical workflow, resulting in designs that depend heavily on iterative simulations or empirical tuning [1], [5]-[10]. Two-stage architectures and current-doubler variations improve performance in specific regions yet introduce extra components and added uncertainties that complicate systematic design and optimization [6], [8], [9]. Research on high-performance DAB, current-fed DAB (CFDAB), and transformer-assisted bridge (TAB) converters has demonstrated strong soft-switching capability and transient performance, especially for wide-voltage platforms [11]-[15]. However, these architectures present their own design-methodology challenges: circulating energy and device-stress characteristics cannot be accurately predicted without detailed multi-variable modeling, and transformer design is often treated independently from resonant-tank behavior or small-signal control stability [11]-[15]. This separation of design domains tank, magnetics, and control limits the ability to generate consistent, end-to-end design rules for EV APMs. LLC-family resonant converters have therefore gained prominence because their behavior can be expressed through normalized frequency-gain relations, enabling high efficiency, ZVS/ZCS operation, and compact magnetic design [6], [16]-[26]. Yet, despite their advantages, the existing literature primarily addresses the LLC design problem in fragments: resonant-tank modeling and gain shaping in isolation [17], [19], [23], [24] transformer design treated as a separate magnetics task [18], [19], [20], [26]control development (PI or LADRC) examined independently from tank-parameter selection [24], [25]; EV-specific constraints (wide input, load variation, transient requirements) discussed qualitatively or addressed only through simulation [16]-[27]. Complementary efforts such as SIMO converters, current-doubler rectifiers, and improved rectification strategies for AHB converters provide subsystem-level improvements but do not resolve the core methodological gap: how to derive resonant-tank parameters, transformer geometry, and small-signal controller gains in one coherent process that guarantees stability, soft switching, and efficiency for EV APMs [6], [8], [9], [18], [28]. Application notes and isolated modeling references provide valuable insights but stop short of a full analytical design-to-implementation pipeline [5], [10], [28]-[31]. Table 1 indicates that existing EV APM converter studies have explored various aspects of converter design, including analytical modeling, control design, and performance evaluation. However, these aspects are generally treated separately, suggesting that a more integrated design approach may further support the systematic development of EV APM converters.

This paper addresses that gap by proposing a unified analytical design methodology for a half-bridge LLC resonant converter tailored to EV APM requirements. The proposed workflow includes (i) A specification-driven resonant-tank selection procedure that uses normalized gain–frequency maps to determine L_n and Q_e while staying within soft-switching regions; (ii) A transformer sizing method derived from core geometry, flux limits, and loss constraints; and (iii) A small-signal-based PI tuning approach that explicitly accounts for the LLC plant's inherent inversion and sets crossover margins accordingly. The workflow is implemented and validated in MATLAB/Simulink and PLECS under EV-relevant operating ranges to verify that the analytical steps translate into predictable behavior in simulation. By linking these three domains through a structured analysis path, the framework reduces reliance on iterative simulations. It produces a converter whose performance voltage regulation, transient behavior, and efficiency is validated across EV-relevant operating conditions. The approach consolidates fragmented design knowledge scattered across the literature [1]–[31] into a single, repeatable procedure suitable for high-confidence EV APM development.

Table 1. Comparative review of EV APM converter analytical design approach

Ref.	Focus/topology	Full analytical design	PI via small-signal	Comparative eval
[16]	T-type LLC	Yes	No	Partial
[25]	LLC analysis/modeling (EV)	Partial	No	No
[10]	PSFB vs LLC	Partial	No	Yes
[19]	GaN LLC	Partial	No	Yes
[17]	Three-leg LLC OBC	Partial	No	Partial
[20]	Full-bridge LLC charger	Partial	No	No
[23]	LADRC vs PI for LLC chargers	No	Yes	Partial
[24]	Current-control methods for LLC	No	Partial	Yes
[8]	Half-bridge + current doubler	Partial	No	Partial
[12]	CFDAB ultra-high-gain APM	Partial	Partial	Yes
[5]	Two-stage isolated DC-DC APM	Partial	No	Partial
[21]	LLCLC notch resonant	Partial	No	Partial
[27]	Asymmetrical half-bridge rectifier	Partial	No	Partial
[18]	LLC high gain with aux LC	Partial	No	Partial

The proposed analytical design process is discussed with a design example of a half-bridge LLC resonant converter where the design specification is for EV APM. The design example is modelled and analysed through MATLAB/Simulink and PLECS simulations under EV-relevant conditions (235–265 V input, 10–100% load), demonstrating peak efficiency of 98.1%, average efficiency around 90%, and output-voltage regulation within ±1%, outperforming a conventional AHB design by up to 4.41%. The typical circuit topology of a half-bridge LLC resonant converter is shown in Figure 1.

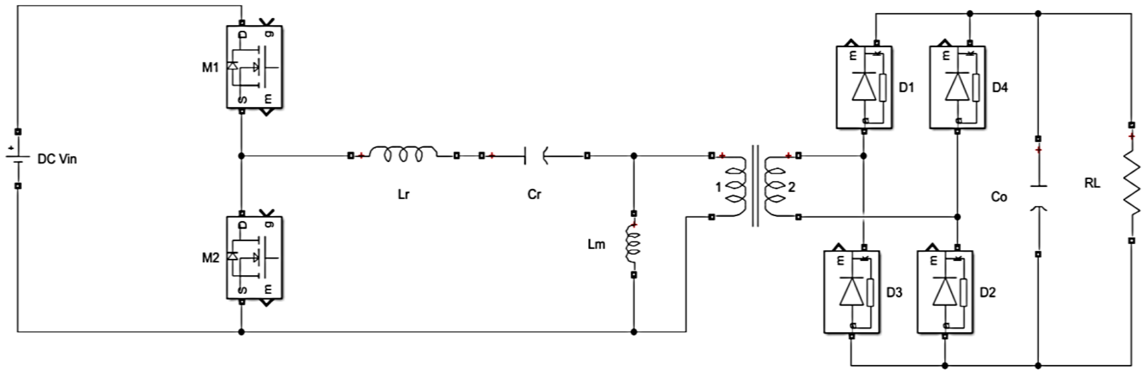

Figure 1. Typical half-bridge LLC resonant converter

2. METHOD

2.1. LLC resonant analytical calculations (design auxiliary components)

The analytical calculation was applied to design the proposed dc-dc LLC resonant converter with the design requirements in Table 2 chosen based on the EV load typical requirements and inferred from documented performances of previous LLC DC-DC converters for EV loads, using the research of [9], [23]. The proposed flow of analytical steps to design the parameters of the LLC converter, as depicted in Figure 1, is simplified as shown in Figure 2.

Table 2. Design specification

Parameters	Value
DC Input voltage, V_{in}	235–265 V
Nominal input voltage, V_{in_nom}	250 V
Rated output power, P_{out}	300 W
Nominal output voltage, V_{o_nom}	24 V
Rated output current, I_o	12.5 A
Ripple current	≤ 1%
Output-voltage ripple	≤ 1%
Expected efficiency	≥ 90% (≈95%)
Switching frequency f_{sw}	70–150 kHz

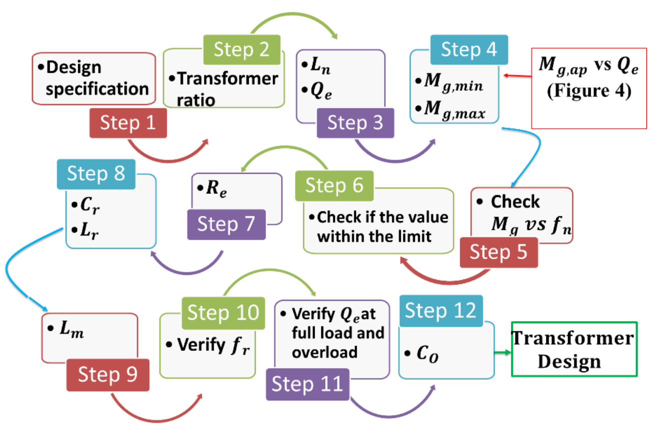

Figure 2. Proposed design steps for an LLC resonant DC-DC converter

The selection of the resonant-tank parameters begins with establishing the transformer turns ratio n at the nominal operating point where (1).

$$n = M_g \times \frac{V_{in\_nom}/2}{V_o} \tag{1}$$

Where M_g is the normalized voltage gain function. The M_g provides a unified, dimensionless representation of how the LLC converter's output voltage relates to its input voltage, thereby enabling simplified analytical design, universal gain-curve construction, operating-region identification (buck, boost, or resonant), soft-switching assessment, and efficient support for modeling, simulation, and optimization.

$$M_g = \left| \frac{L_n \times {f_n}^2}{[(L_n+1) \times {f_n}^2 - 1] + j[({f_n}^2-1) \times f_n \times Q_e \times L_n]} \right| \tag{2}$$

Where the normalized frequency f_n is the ratio of the f_{sw} and the resonant frequency f_0. The quality factor Q_e of the series resonant circuit is the ratio of energy stored in the resonant tank to the energy dissipated per cycle at the resonant frequency.

$$Q_e = \frac{\sqrt{L_r/C_r}}{R_e} \tag{3}$$

A small induction ratio L_n where the transformer magnetizing inductance L_m is smaller than the resonance inductance L_r enhances ZVS but increases losses due to higher magnetizing current, while a small Q_e likewise raises losses. Thus, the proper ranges of L_n and Q_e have to be determined. The L_n and Q_e can be predicted by plotting the graph of M_g against f_n as depicted in Figure 3. The chosen sets for the $L_n$is 1, 3, 5, 6, 8 and 10 while the Q_e is {0, 0.2, 0.3, 0.4, 0.5, 0.7, 1, 1.2, 10}. The minimum voltage gain $M_{g,min}$ and maximum voltage gain $M_{g,max}$ are the range of $M_g$for the load voltage V_o regulation. Referring to Figure 3, the peak of each curve $M_{g,peak}$ are in the capacitive region where is the ZVS cannot be achieved. Therefore, the maximum attainable gain $M_{g,ap}$ is estimated to be 1% less than $M_{g,peak}$ to ensure ZVS. However, for $M_{g,peak}$ less than $M_{g,max}$, the load voltage regulation cannot be achieved. Hence, by observing the plotted curves in Figure 3, the curves below the red dotted line are not considered in determining the L_n and Q_e because $M_{g,peak}$ less than $M_{g,max}$. Next, the $M_{g,ap}$ against $Q_e$is plotted as shown in Figure 4, where the value of Q_e is chosen such that $M_{g,ap} > M_{g,max}$. In addition, the L_n cannot be too small, as this would increase the magnetizing current I_m, leading to higher power losses and Q_e should not be too small to avoid excessive switching losses. Therefore, in this study, the $L_n = 5$ and $Q_e = 0.53367$ are selected as depicted in Figure 5, where the range of switching frequency f_{sw} is between the $f_{n,min}$ and $f_{n,max}$. Next, the value of an equivalent ac resistance R_e is determined from the of (4).

$$R_e = \frac{8 \times n^2}{\pi^2} \times \frac{V_o}{I_o} \tag{4}$$

Consequently, the values of resonant circuit components are designed based on (5)-(7).

$$C_r = \frac{1}{2\pi R_e f_0 Q_e} \tag{5}$$

$$L_r = \frac{1}{(2\pi f_o)^2 \times C_r} \tag{6}$$

$$L_m = L_n L_r \tag{7}$$

Next, the designed values for resonance circuit components are verified by repeating the same step from (5) to (7), and the L_n. The updated curve M_g vs f_n as in Figure 6 is plotted. This is to ensure that the $M_{g,peak}$ less than $M_{g,max}$ and satisfies the M_g and Q_e criteria for the resonant circuit design. In addition, the $f_{n,min}$ and $f_{n,max}$ are observed to be between the design specifications. Thus, the range of switching frequency is determined.

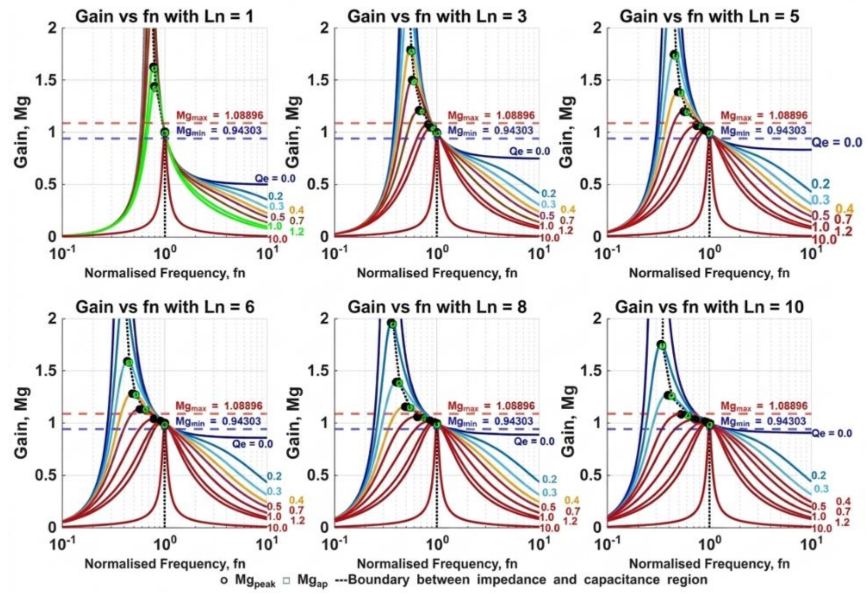

Figure 3. M_g vs f_n

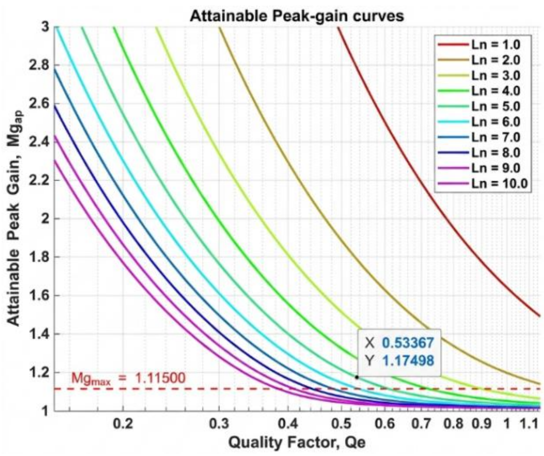

Figure 4. $M_{g,ap}$ against Q_e

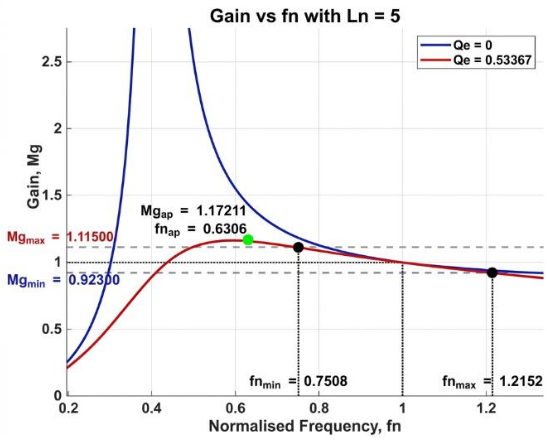

Figure 5. M_g vs f_n for $L_n = 5$

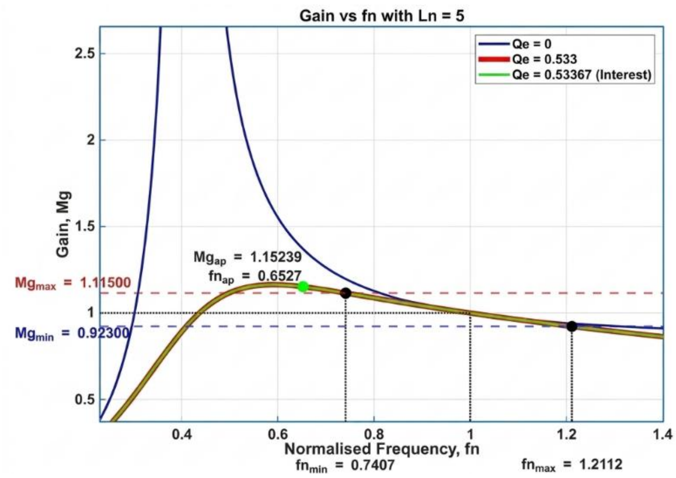

Figure 6. Updated M_g vs f_n for $L_n = 5$

The transformer magnetizing inductance R_c is part of the resonant circuit. Thus, the initial transformer core losses have to be predetermined. The analytical design for the transformer is based on the [26] report. At the secondary side, the value of the minimum output capacitor is (8).

$$C_{o,min} = \frac{I_{OUT}\times D\times(1-D)\times 1000}{f_{sw}\times V_{P(max)}} \tag{8}$$

The analytical design for components is then applied to the simulation model in MATLAB Simulink and PLECS as depicted in Figures 7 and 8.

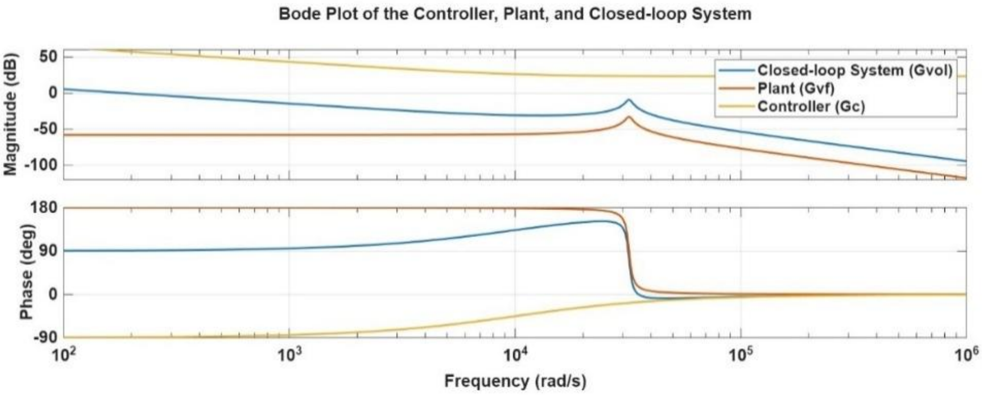

Figure 7. The Bode plot for the proposed circuit, PI controller, and proposed circuit with PI

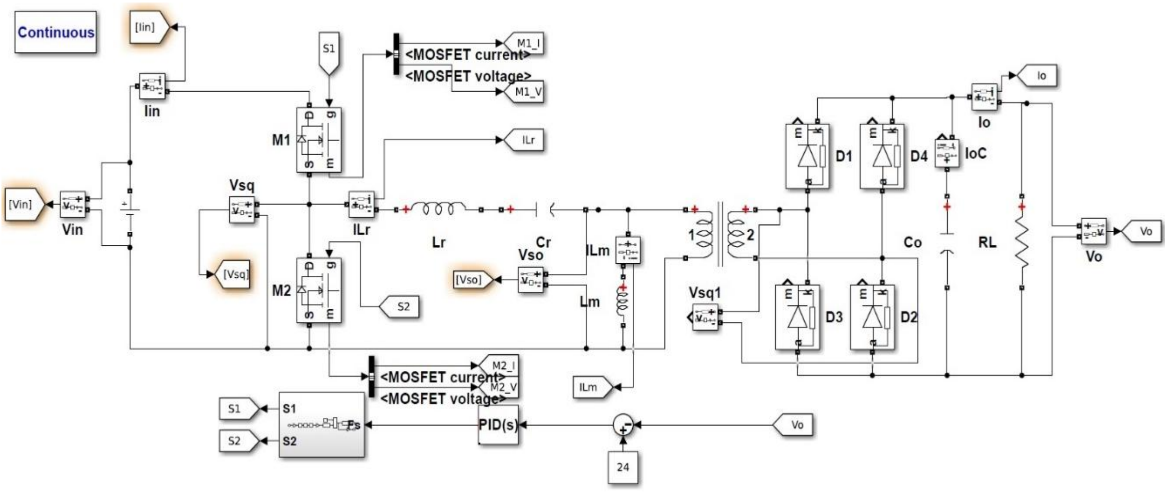

Figure 8. Proposed Simulink model

2.2. Transformer design

The proposed design process of the transformer is shown in Figure 9. In order to simplify the design process, the core manufacturer data handbook is referred to in selecting the core type and core material. The pre-requisite requirements to choose the core are the switching frequency f_{sw} and the expected output power P_o. Thus, referring to the Ferroxcube Data Handbook, the core material of 3C90 and the predetermined core shape of ETD44 are chosen. The ETD core is chosen because ETD cores have a round center post that allows for shorter turn length by almost 11%, hence leading to a copper loss reduction. Next, the core loss coefficient K_{fe} is determined from (9).

$$P_{fe} = K_{fe}(B_{max})^{\beta} A_c l_m \tag{9}$$

Where P_{fe} is the core losses, A_c is the core sectional area and l_m is the magnetic path length, which is extracted from the core datasheet. The typical value of the core loss exponent β typically between 2.6-2.8. The maximum flux density B_{max} is determined from the graph of fB_{max}vs f_{sw} core material datasheet. Next, the suitability of the selected core size is verified by observing the value of the geometric constant k_{gfe}, where is (10).

$$k_{gfe} = \frac{\rho\lambda_1{}^2 I_{tot}{}^2 K_{fe}{}^{(2.\beta)}}{4K_u(P_{tot})^{((\beta+2)/\beta)}} \times 10^8 \quad (10)$$

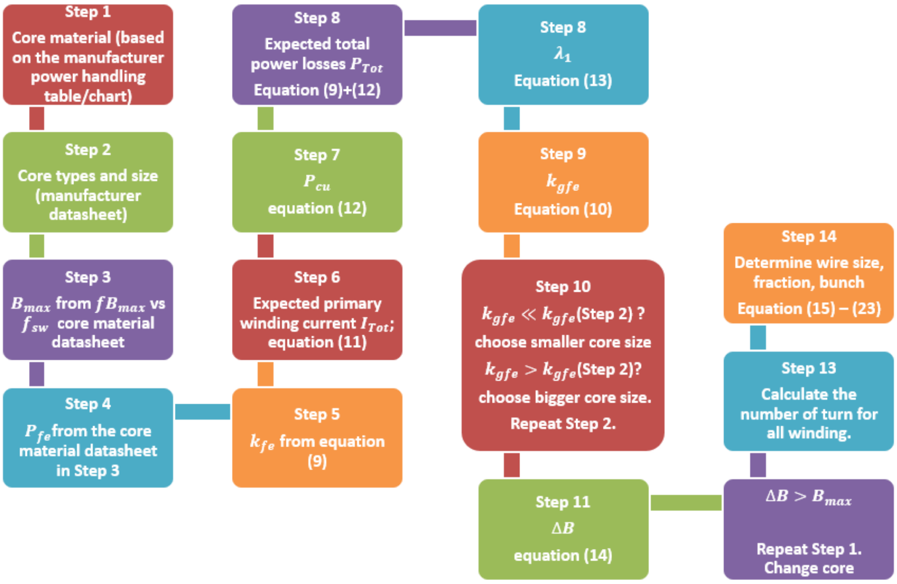

Figure 9. Proposed simplified transformer design flow

The typical value of effective wire resistivity ρ = 1.724×10^{-6} Ω-cm and the winding fill factor $K_u$is 0.25-0.3. The expected total primary side rms winding current I_{tot} can be obtained from (11).

$$I_{tot} = \frac{\pi}{2\sqrt{2}} \times \frac{1}{n} \times I_o \quad (11)$$

P_{tot} is the allowable total power dissipation which is the sum of the core P_{fe} and copper losses P_{cu}. Thus, the copper losses P_{cu} is (12).

$$P_{cu} = \left(\frac{\rho\lambda_1{}^2 I_{tot}{}^2}{4K_u}\right)\left(\frac{MLT}{W_A A_c{}^2}\right)\left(\frac{1}{\Delta B}\right)^2 \quad (12)$$

Where W_A is core window area, MLT is mean length per turn and $\lambda_1$is the applied primary volt-second during the positive portion of arbitrary periodic primary voltage. which is (13).

$$\lambda_1(t) = \int_{t_1}^{t_2} v_1(t)\,dt \quad (13)$$

Thus, the geometric constant k_{gfe} for this study is 10.4×10^{-3} which is smaller than k_{gfe} for ETD44 core 30.4×10^{-3}. Therefore, the smaller ETD core can be used. However, in this work, ETD44 is used because of its availability. Next, the peak flux density, ΔB has to be below the B_{max} to ensure no saturation.

$$\Delta B = \left[\frac{\rho\lambda_1{}^2 I_{tot}{}^2}{2K_u}\frac{(MLT)}{W_A A_c{}^3 l_m}\frac{1}{\beta K_{fe}}\right]^{\left(\frac{1}{\beta+2}\right)} \quad (14)$$

The ΔB is 106.6 mT which is below B_{max}, 200 mT. Therefore, the core material 3C90 is safe to be used for this study. The primary number of turns is determined to be (15),

$$N_1 = \frac{\lambda_1}{2\Delta B A_c} 10^4 \tag{15}$$

and for the secondary winding N_2, is determined with the transformer transformation ratio n. Next is to determine the number of fractions α_k. α_k is the space within the core where the windings are placed. Since there are two windings (primary and secondary) for the transformer in this work, therefore by (16).

$$\alpha_1 = \frac{N_1 I_1}{N_1 I_{tot}}, \alpha_2 = \frac{N_2 I_2}{n_1 I_{tot}} \tag{16}$$

The cross-sectional area for the primary $A_{w1}$and secondary A_{w2} are evaluated using (17).

$$A_{w1} \leq \frac{\alpha_1 K_u W_A}{n_1}, A_{w2} \leq \frac{\alpha_2 K_u W_A}{n_2} \tag{17}$$

Where W_A is the bobbin winding area, which can be determined from the coil former data sheet. Next, the wire size for $N_1$and N_2 are determined by comparing the value of A_{w1} and A_{w2} with the American Wire Gauge (AWG) table. Once the wire size is determined, the transformer magnetizing inductance L_M, primary winding resistance $R_1$and secondary winding resistance $R_2$are

$$L_M = \frac{\mu {n_1}^2 A_c}{l_m} \tag{18}$$

$$R_1 = \frac{\rho n_1 (MLT)}{A_{w1}} \tag{19}$$

$$R_2 = \frac{\rho n_2 (MLT)}{A_{w2}} \tag{20}$$

Even though the wire size is determined from (17) and the AWG table, further consideration of power losses due to the skin effect and proximity effect with a stranded wire is shown in Figure 10.

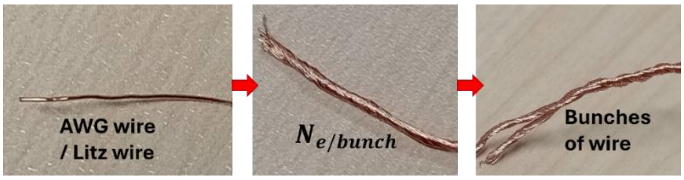

Figure 10. Stranded wire for the transformer winding

Hence, the number of strands n_e is (21).

$$n_e = k \frac{\delta^2 b}{N_s} \tag{21}$$

Where the constant k is the packing factor, which accounts for the strands in the available space. The simplified values of k can be found in the litz wire documents from the manufacturer. The breadth b is the sum of half of the winding width and the winding leg diameter. $N_s$is the number of turns of the winding and the skin effect δ is (22),

$$\delta = \sqrt{\frac{\rho}{\pi f_{sw,max} \mu}} \tag{22}$$

and μ is the permeability of copper. Where the breadth b is the sum of half the winding width and the winding leg diameter. Once the n_e are determined, the $n_e$is bunch in a group. The maximum number of wires in a group $N_{e/bunch}$ is (23).

$$N_{e/bunch} = 4 \frac{\delta^2}{{d_s}^2} \tag{23}$$

2.3. Controller

The small signal model for the LLC converter proposed by [9] is used to model the control loop, where the control-to-voltage transfer function is (24),

$$G_{vf}(s) = \frac{v_{Co}(s)}{f_s(s)} = \frac{\frac{k_f}{n}}{\frac{C_o L_{eq}}{n^2}s^2 + \frac{L_{eq}}{n^2 R_L}s + 1} \tag{24}$$

where the dynamic small-signal gain.

$$k_f = \frac{\partial v_o}{\partial f_s} = -\frac{8V_{in}L_m}{\pi n L_r f_f} \tag{25}$$

$$L_{eq} = \frac{n^2 C_r}{C_o} \frac{\pi^2 L_r}{\cos^{-1}[\frac{C_o}{C_o + n^2 C_r (1 - \frac{n^2 C_r}{C_o})}]^2} \approx \frac{\pi^2}{4} L_r \tag{26}$$

$$f_{eq} = \frac{n}{2\pi\sqrt{L_{eq}C_o}} \tag{27}$$

The Bode plot based on the design specifications and with compensation is shown in Figure 7. At the natural frequency (representing the resonant frequency at the output filter), ω_o, is (28).

$$\omega_o = \frac{n}{\sqrt{C_o L_{eq}}} \tag{28}$$

The quality factor Q is (29).

$$Q = nR_L\sqrt{\frac{C_o}{L_{eq}}} \tag{29}$$

The negative small-signal gain k_f introduces an inherent 180° phase inversion, and the plant exhibits−23.25 dB gain at the crossover region, requiring additional phase and gain compensation for the loop to reach the 0 dB stability condition. A PI controller is therefore selected and tuned so that the compensated crossover frequency remains well below the minimum switching frequency, satisfying the Nyquist stability requirement.

2.4. Robustness and analysis

The robustness of the proposed LLC converter was evaluated by observing how the resonant tank responds to input-voltage variations and load changes. The converter was simulated at 235 V, 250 V, and 265 V to examine changes in resonant-tank voltage, current, and switching frequency, allowing assessment of how the controller maintains the operating point under off-nominal conditions. For each input level, the resonant frequency and current amplitude were recorded, and the corresponding waveforms were analyzed to confirm that tank behavior follows the expected analytical trends. The output voltage and current were then monitored to verify that the design specifications were met, and the mode of operation was validated by comparing switching waveforms from both the Simulink and PLECS models.

Performance across the EV-relevant load range was further assessed by sweeping the load from 10% to 100% and computing the efficiency and voltage-regulation characteristics, using PLECS simulations to cross-validate the results obtained from Simulink. Load-transient robustness was evaluated by applying sudden step changes, where the settling time of the output voltage was measured to confirm the controller's dynamic response. Finally, the efficiency profile of the proposed converter was compared against that of a conventional AHB topology to quantify performance advantages, and the consistency between MATLAB and PLECS results ensured reliability of the simulation model and its analytical foundation.

3. RESULTS AND DISCUSSION

Table 3 shows the quantities for the LLC converter which derived from the analytical design as depicted in the flow chart of Figure 2. The Bode plot in Figure 7 shows that the controller provides high dc gain while the plant exhibits negative low-frequency gain, resulting in a positive open-loop response with a crossover near 204 rad/s and adequate PI-type stability margin as all curves roll off smoothly at high frequency. Applying the tuned k_p and k_i in Simulink and PLECS (Figures 8 and 11) produces nearly identical switching waveforms (Figure 12), confirming correct operation of the proposed design.

Next, for the analytical design of the transformer as depicted in Figure 9, the summarized quantities are shown in Table 4. The arrangements of the primary winding and secondary winding based on ETD44 bobbin winding width, winding direction, and the actual construction of the transformer are shown in Figure 13. Figure 14 shows that increasing the input voltage raises the switching frequency from about 93 kHz at 235 V to 130 kHz at 250 V, which remains which satisfies the resonant circuit design requirement. However, at 265 V, the frequency rises to approximately 275 kHz, exceeding the allowable limit, indicating that the controller requires refinement to keep the switching frequency within the specified operating band.

The analysis-first process normalized gain–frequency synthesis for tank parameters, analytical transformer design (ETD44/3C90 with ΔB = 106.6 mT < 200 mT), and small-signal-based PI tuning produces a coherent design whose Simulink and PLECS implementations match in switching patterns and operating points (Figures 8-14). This consistency validates the end-to-end methodology, not only the individual components. The close similarity between the MATLAB Simulink and PLECS waveforms shows that the model represents the resonant-tank behavior and the small-signal response of the LLC converter effectively. This agreement also indicates that the analytical design transfers well into both simulation platforms without the need for parameter adjustments, supporting the use of a consistent and reliable analytical-to-simulation workflow.

Table 3. Quantities of the proposed circuit derived from the analytical design

Quantities	Values	Quantities	Values
n	5	k_f	−005.901
$M_{g,min}$	0.923	R_e	38.9 Ω
$M_{g,max}$	1.115	C_r	276.6 nF
V_{loss}	1.263	L_r	33 μH
L_n	5	Q	58.28
Q_e	0.533	K_p	14.54
L_m	165 μH	K_i	147116.6
f_{sw}(kHz)	80.6~128.3	$f_{n,max}$	1.1532
$C_{o,min}$	312.5 μF	$f_{n,min}$	0.7968
L_{eq}	8.14 μH	ω_o(kHz)	100.038
f_{eq}	16.1 kHz	Q	58.28

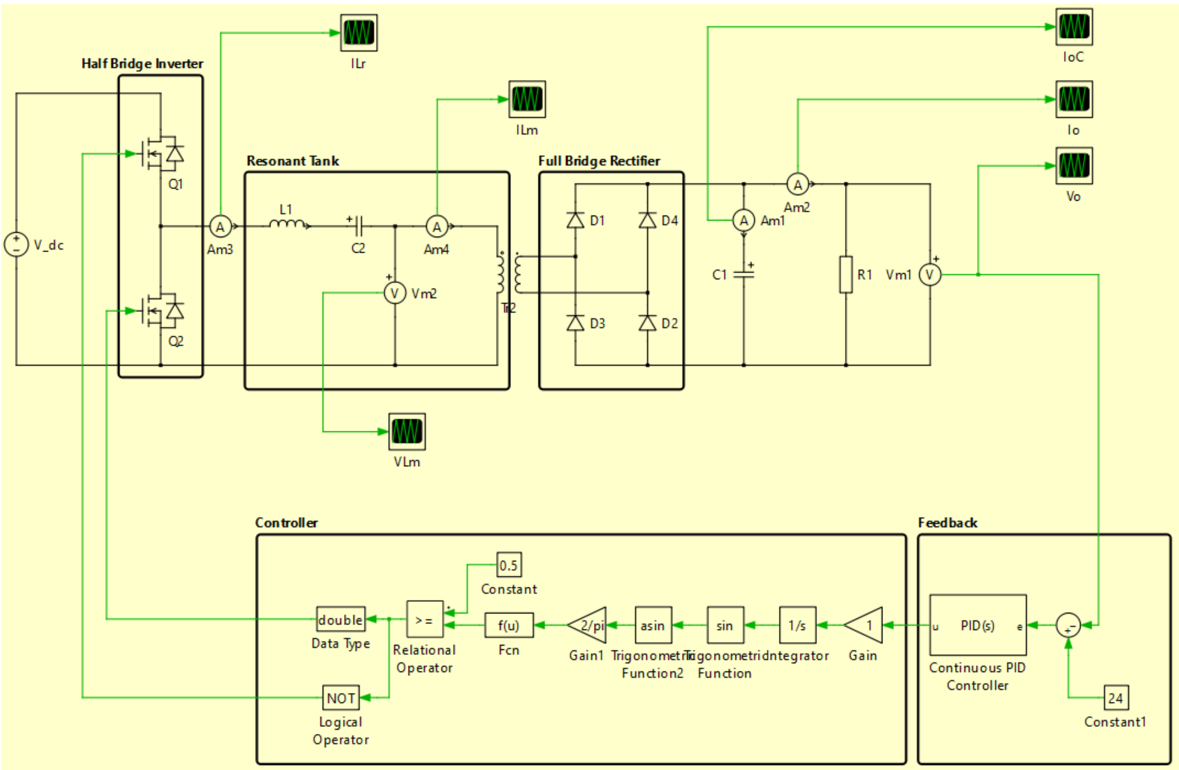

Figure 11. Proposed PLECS model

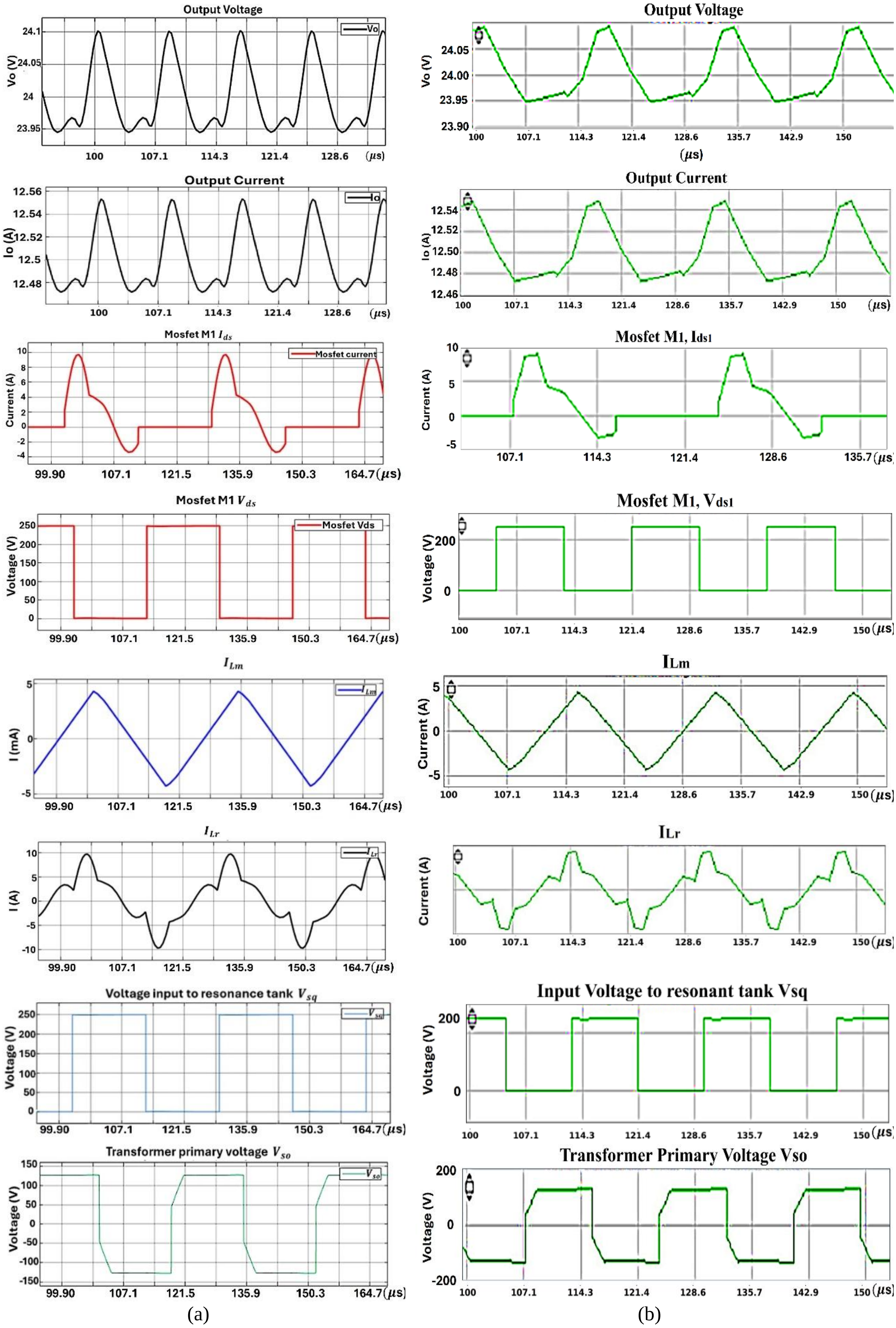

Figure 12. Switching waveform simulated through MATLAB: (a) Simulink and (b) PLECS

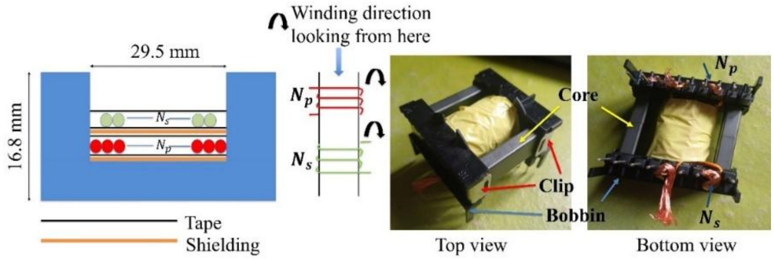

Figure 13. Construction of the transformer

Table 4. The summary for the quantities of transformer design by analytical method

Parameter	Value	Parameter	Value
Core material	3C90	Core loss coefficient (Kfe)	1.831 W/(cm³·T$^{2.7}$)
Core shape	ETD	Core loss (Pfe)	0.07585 W
Core size	ETD44	Copper loss (Pcu)	0.2199 W
Cross-sectional area (Ac)	1.74 cm²	Total loss (Ptot)	0.2958 W
Mean length per turn (MLT)	7.62 cm	Primary turns (n_1)	17
Magnetic path length (lm)	10.3 cm	Secondary turns (n_2)	3.5
Bobbin winding area (WA)	2.13 cm²	Window area fraction (primary)	0.5
Geometrical constant (Kgfe)	30.4×10^{-3}	Window area fraction (secondary)	0.514
Thermal resistance	12 °C/W	Wire size (primary)	AWG #16
Operating frequency (fsw)	100 kHz	Wire size (secondary)	AWG #9
Duty cycle (D)	50%	Current density (primary)	2.12 A/mm²
Primary RMS voltage (Vc1)	125 V	Current density (secondary)	2.09 A/mm²
Primary RMS current	2.776 A	Skin depth (δ)	0.1945 mm
Secondary RMS current	13.88 A	Litz wire strand size	AWG 38
Performance factor	20,000 Hz·T	Strands (primary)	33 strands (5×3×2 config)
Maximum flux density (Bmax)	200 mT	Strands (secondary)	140 strands (5×3×9 config)
Peak flux density (ΔB)	106.6 mT		

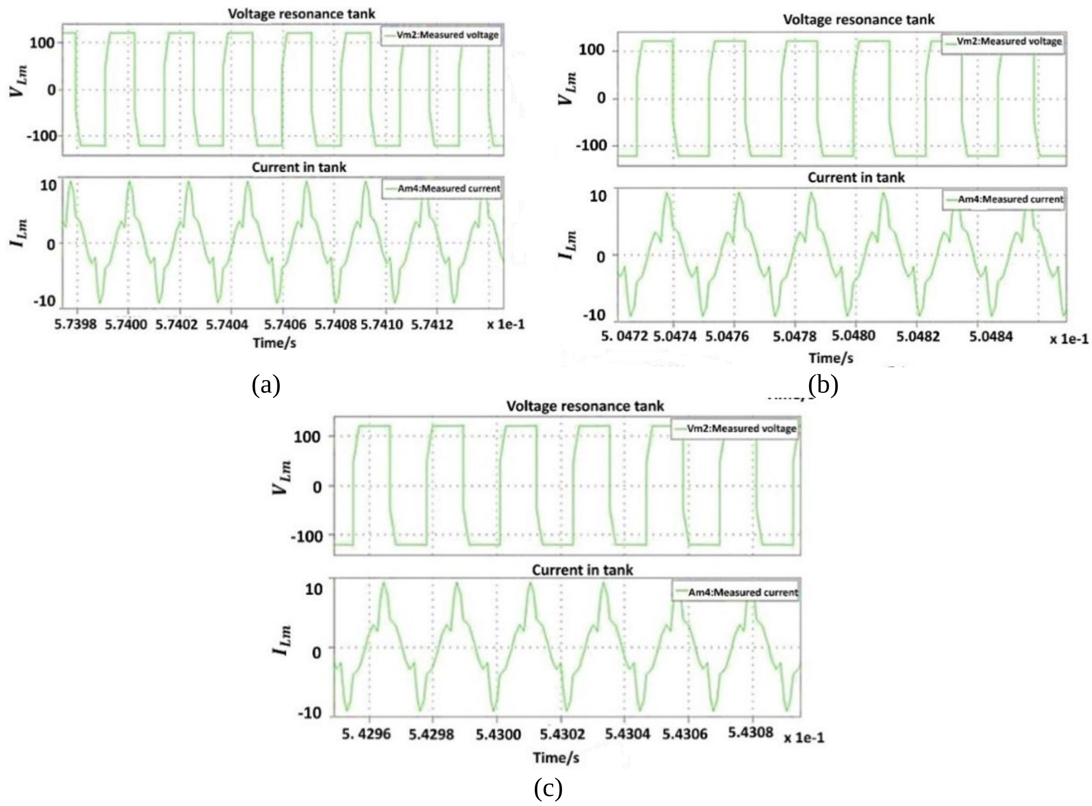

Figure 14. Voltage and current behavior of the resonant tank at the input voltage:
(a) 235 V, (b) 250 V, and (c) 265 V

Efficiency and ZVS: Across 235–265 V and 10–100% load, the proposed HB–LLC attains a peak efficiency of 98.1% and an average near 90%, as depicted in Figures 15 and 16. These values follow from the tank selection ($L_n = 0.5$, $Q_e \approx 0.53$), which maintains operation in the inductive region where ZVS is realized and circulating energy is reduced; switching waveforms from both Simulink and PLECS confirm ZVS under nominal and off-nominal points. At 265 V, the controller commands $f_{sw} \approx 275$ kHz, exceeding the 150 kHz design ceiling; this behavior indicates a control-band constraint rather than a tank limitation and can be mitigated by imposing an f_{sw} cap, slightly increasing f_o, or adjusting Q_e to shift the required gain into the admissible band. The observed performance directly validates the proposed analytical design methodology, as every major operating characteristic ZVS, regulation quality, switching-frequency range, and efficiency arises from the analytically selected (L_n, Q_e, f_o) rather than empirical tuning, demonstrating that the design process described in the title is both predictive and reliable for EV-APM requirements

Next, the load voltage regulation was examined to evaluate the effectiveness of the designed controller. Figure 17 shows the waveforms of the V_o and I_o during sudden load changes from 100% to 80% of load, and vice versa. The V_o remains approximately constant. The closed-loop system meets the ±1% regulation (Figure 18) target throughout most of the operating space, with 0.42–0.44 ms settling for 100%↔80% load steps. The worst observed corner (235 V, 10% load) dips to approximately 23 V (≈4.17% deviation), which occurs when the f_{sw} departs substantially from f_o to satisfy the required gain at light load. This can be corrected by minor PI retuning and by adding voltage feedforward or a lead term to improve frequency tracking away from resonance. The efficiency profile (peak 98.1%, average ≈90%) and regulation robustness (±1% under load change with 0.42–0.44 ms settling) demonstrate that the analytically designed converter satisfies EV-APM operating constraints, thereby confirming the application relevance stated in the title.

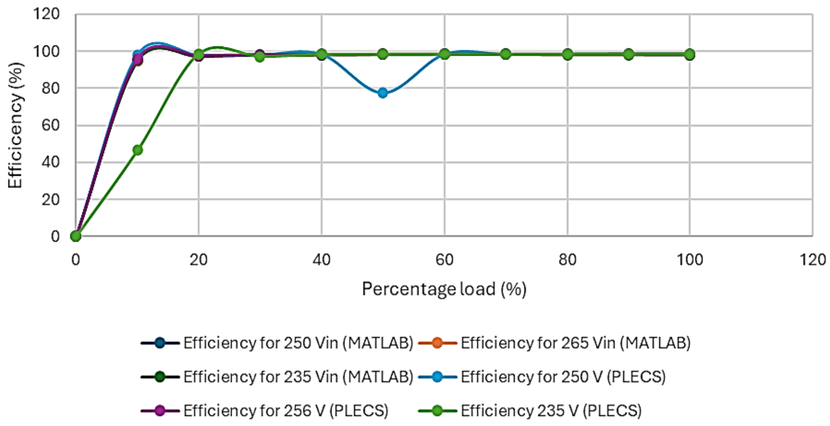

Figure 15. Power conversion efficiency across the load and the range of supply voltage

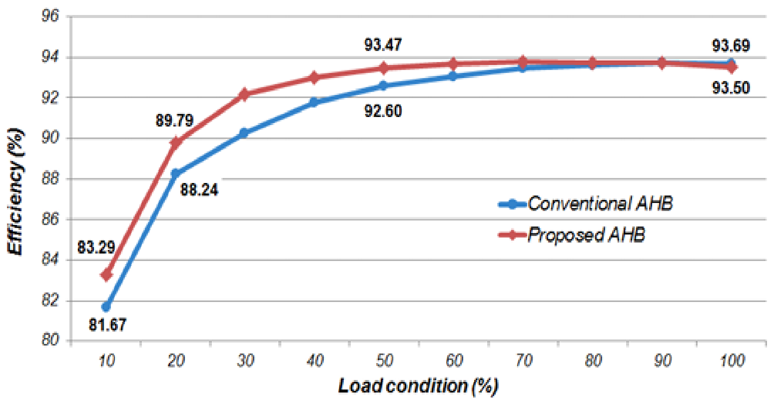

Figure 16. Comparison of the power conversion efficiency across the load between the proposed AHB and the conventional AHB

The experimental verification process, which involves transitioning from a simulation model to a physical circuit design, requires additional considerations to bridge the gap between theory and practical implementation. These include component tolerances, switching device characteristics, and thermal management, all of which significantly affect power conversion efficiency. Furthermore, proper printed circuit board (PCB) design techniques are essential to minimize stray inductance, which can otherwise increase total power losses. The experimental verification, including circuit design, PCB layout, testing procedures, and robustness analysis, will be discussed in detail in the next report.

Overall, the results verify the analytically derived resonant-tank parameters, transformer design, and control gains collectively produced a converter that meets EV-APM requirements, confirming the validity of the proposed analytical design methodology. The modelling approach is validated by consistent dual-platform simulations, and the efficiency and regulation performance relative to the AHB benchmark substantiate the novelty and practical relevance of the proposed framework.

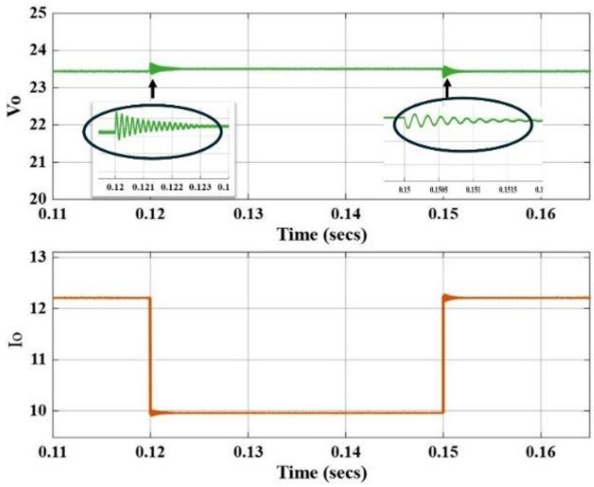

Figure 17. Output voltage and current waveform for load changes, 100% load to 80% vice versa

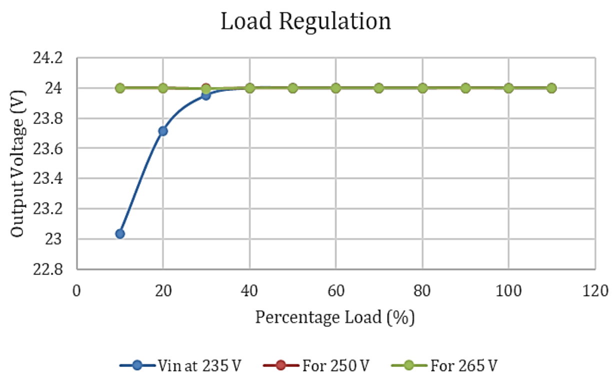

Figure 18. Output voltage regulation across the load within the range of input voltage

4. CONCLUSION

The analytical design approach for the LLC resonant converter and the transformer design have been discussed, supported by a proposed flowchart and a practical example based on APM EV requirements. The method integrates resonant tank synthesis, transformer design, and small signal PI tuning into a unified process. The workflow is implemented and cross-validated in MATLAB/Simulink and PLECS, confirming that the analytical steps translate into predictable simulation behavior. Simulation results from MATLAB/Simulink and PLECS confirm stable operation, ZVS, ±1% voltage regulation, fast load-step recovery, and peak efficiency of 98.1% with an average near 90%. Under identical conditions, it shows a 4.41% peak-efficiency advantage over a conventional AHB baseline. These results confirm the proposed single analysis-first process that links tank design, transformer design, and controller tuning in a structured and predictable way, reducing the need for iterative trial-and-error during development. However, the proposed analytical design process with design example was validated without the constraint of PCB parasitic, thermal coupling, EMI, and tolerance which will only verify experimentally. Hardware prototype will be built to implement the analytical tank design, transformer sizing, and PI controller, and to measure the performance, with PCB-level EMI and thermal tests compared against the MATLAB/Simulink and PLECS models. Based on any gaps observed, the workflow will be refined by adding constraint-aware limits on switching frequency and making small controller adjustments. Overall, the end-to-end analytical workflow and its verified efficiency and regulation benefits provide a clear path from analysis to implementation.

ACKNOWLEDGMENTS

Author would like to thank the management of Asia Pacific University of Technology and Innovation for the encouragement and financial support.

FUNDING INFORMATION

The authors acknowledge that funding was provided by Strategic Research Institute, Asia Pacific University of Technology and Innovation, solely to cover the publication fee for this article. No additional financial support was received for the research or authorship of this work.

AUTHOR CONTRIBUTIONS STATEMENT

This journal uses the Contributor Roles Taxonomy (CRediT) to recognize individual author contributions, reduce authorship disputes, and facilitate collaboration.

Name of Author	C	M	So	Va	Fo	I	R	D	O	E	Vi	Su	P	Fu
Mohamad Affan Mohd Noh	✓	✓	✓	✓	✓	✓		✓	✓	✓			✓	
Jacques Juicy Patureau Ravina		✓	✓		✓	✓		✓	✓		✓			
Sivakumar Sivanesan	✓						✓			✓			✓	
Hafizul Azizi Ismail	✓							✓		✓		✓		
Ali Akbar Firoozi					✓					✓				

C : **C**onceptualization
M : **M**ethodology
So : **So**ftware
Va : **Va**lidation
Fo : **Fo**rmal analysis
I : **I**nvestigation
R : **R**esources
D : **D**ata Curation
O : Writing - **O**riginal Draft
E : Writing - Review & **E**diting
Vi : **Vi**sualization
Su : **Su**pervision
P : **P**roject administration
Fu : **Fu**nding acquisition

CONFLICT OF INTEREST STATEMENT

The authors declare that there is no conflict of interest regarding the publication of this article.

DATA AVAILABILITY

Derived data supporting the findings of this study are available from the corresponding author [MAMN], on request.

REFERENCES

[1] C. Wang, P. Zheng, and J. Bauman, "A review of electric vehicle auxiliary power modules: challenges, topologies, and future trends," *IEEE Transactions on Power Electronics*, vol. 38, no. 9, pp. 11233–11244, Sep. 2023, doi: 10.1109/TPEL.2023.3288393.

[2] M. Bassey, "Adoption of electric vehicles (Evs) as a sustainable transportation solution: reshaping the trends in conventional automobile applications," In *Adoption of Electric Vehicles (EVS) As A Sustainable Transportation Solution: Reshaping The Trends In Conventional Automobile Applications*, 2024, pp. 1–28.

[3] F. Alanazi, "Electric vehicles: benefits, challenges, and potential solutions for widespread adaptation," *Applied Sciences*, vol. 13, no. 10, p. 6016, May 2023, doi: 10.3390/app13106016.

[4] van-C. Bui, K. M. Nguyen, D. T. Duong, D. Vo, Y.-C. Lim, and J.-H. Choi, "An isolated DC-DC converter for 800 V electric vehicle with wide soft-switching range and low voltage stress on power switches," *IEEE Access*, vol. 12, pp. 159473–159487, 2024, doi: 10.1109/ACCESS.2024.3487233.

[5] P. H. B. Löbler, W. G. R. Volz, A. Toebe, C. Rech, and L. Schuch, "A two-stage isolated DC-DC architecture for EV auxiliary power module," in *IECON 2025 – 51st Annual Conference of the IEEE Industrial Electronics Society*, Oct. 2025, pp. 1–6, doi: 10.1109/IECON58223.2025.11221013.

[6] R. Kotb, S. Chakraborty, D.-D. Tran, E. Abramushkina, M. El Baghdadi, and O. Hegazy, "Power electronics converters for electric vehicle auxiliaries: State of the art and future trends," *Energies*, vol. 16, no. 4, p. 1753, Feb. 2023, doi: 10.3390/en16041753.

[7] M. Dhananjaya, D. Potnuru, P. Manoharan, and H. H. Alhelou, "Design and implementation of single-input-multi-output DC-DC converter topology for auxiliary power modules of electric vehicle," *IEEE Access*, vol. 10, pp. 76975–76989, 2022, doi: 10.1109/ACCESS.2022.3192738.

[8] P. H. B. Löbler, A. Toebe, C. Rech, and L. Schuch, "Analysis of the half-bridge converter with current doubler for application in an auxiliary power module of electric vehicles," in *2023 IEEE 8th Southern Power Electronics Conference and 17th Brazilian Power Electronics Conference (SPEC/COBEP)*, Nov. 2023, pp. 1–6, doi: 10.1109/SPEC56436.2023.10407635.

[9] A. Akash and M. Sreejeth, "Isolated DC-DC converter with synchronous rectification for electric vehicle battery charging," in *2023 3rd International Conference on Intelligent Technologies (CONIT)*, Jun. 2023, pp. 1–5, doi: 10.1109/CONIT59222.2023.10205613.

[10] Jiangheng Lu and A. Khaligh, "1kW, 400V/12V high step-down DC/DC converter: Comparison between phase-shifted full-bridge and LLC resonant converters," in *2017 IEEE Transportation Electrification Conference and Expo (ITEC)*, Jun. 2017, pp. 275–280, doi: 10.1109/ITEC.2017.7993284.

[11] H. Ataullah *et al.*, "Analysis of the dual active bridge-based DC-DC converter topologies, high-frequency transformer, and control techniques," *Energies*, vol. 15, no. 23, p. 8944, Nov. 2022, doi: 10.3390/en15238944.

[12] L. Zhu, H. Bai, and A. Brown, "Model and control of a current-fed dual active bridge based ultrawide-voltage-range auxiliary power module for 400 V/800 V electric vehicles," *IEEE Transactions on Power Electronics*, vol. 39, no. 3, pp. 3263–3276, Mar. 2024, doi: 10.1109/TPEL.2023.3337712.

[13] H. Choi, J. Lee, Y. Cho, and J. Jung, "Design consideration of efficiency improvement in three phase dual active bridge converter for LVDC application," in *2017 IEEE International Telecommunications Energy Conference (INTELEC)*, Oct. 2017, pp. 549–555, doi: 10.1109/INTLEC.2017.8214194.

[14] L. Zhu, H. Bai, A. Brown, and A. Körner, "An ultra-high gain current-fed universal auxiliary power module for 400V/800V electric vehicles," in *2023 IEEE Applied Power Electronics Conference and Exposition (APEC)*, Mar. 2023, pp. 885–891, doi: 10.1109/APEC43580.2023.10131628.

[15] R. Hou and A. Emadi, "Dual active bridge-based full-integrated active filter auxiliary power module for electrified vehicle applications with single-phase onboard chargers," in *2016 IEEE Applied Power Electronics Conference and Exposition (APEC)*, Mar. 2016, pp. 1300–1306, doi: 10.1109/APEC.2016.7468036.

[16] W. Ma, H. Li, S. Yin, X. Pang, and D. Chu, "Design of hybrid SiC/Si based T-type three-level LLC$ LLC$ resonant converter with wide-input range and low conduction loss for automotive auxiliary power module," *IET Power Electronics*, vol. 16, no. 2, pp. 209–226, Feb. 2023, doi: 10.1049/pel2.12377.

[17] B. Vinusha, M. Vinod, D. Kishan, and R. Kalpana, "Analysis of integrated on-board charger for 400 V and 800 V EV battery using dual-mode three-leg LLC resonant converter," in *2024 IEEE International Conference on Power Electronics, Drives and Energy Systems (PEDES)*, Dec. 2024, pp. 1–5, doi: 10.1109/PEDES61459.2024.10961344.

[18] D.-K. Kim, C.-O. Yeon, J.-H. Kim, Y. Jeong, and G.-W. Moon, "LLC resonant converter with high voltage gain using auxiliary LC resonant circuit," in *2015 9th International Conference on Power Electronics and ECCE Asia (ICPE-ECCE Asia)*, Jun. 2015, pp. 1505–1512, doi: 10.1109/ICPE.2015.7167978.

[19] M. Faizan, X. Wang, and M. Z. Yousaf, "Design and comparative analysis of an ultra-highly efficient, compact half-bridge LLC resonant GaN converter for low-power applications," *Electronics*, vol. 12, no. 13, p. 2850, Jun. 2023, doi: 10.3390/electronics12132850.

[20] M. Israr and P. Samuel, "Study and design of DC-DC LLC full bridge converter for electric vehicle charging application," in *2023 5th International Conference on Power, Control & Embedded Systems (ICPCES)*, Jan. 2023, pp. 1–6. doi: 10.1109/ICPCES57104.2023.10076234.

[21] Y. Yuan, L. Xu, C. Yao, J. Yuan, X. Wang, and X. Ruan, "Simplified time-domain design methodology for LLC resonant converter in EV charging station application," in *2024 3rd International Conference on Power Systems and Electrical Technology (PSET)*, Aug. 2024, pp. 332–337, doi: 10.1109/PSET62496.2024.10808767.

[22] S. Bashir and X. Wu, "Time domain modelling of LLC converter," in *2023 IEEE 14th International Symposium on Power Electronics for Distributed Generation Systems (PEDG)*, Jun. 2023, pp. 358–364, doi: 10.1109/PEDG56097.2023.10215302.

[23] H. Bai, D. Yang, J. Song, Q. Su, B. Duan, and C. Zhang, "Linear active disturbance rejection control of LLC resonant converters for EV chargers," in *2020 Chinese Automation Congress (CAC)*, Nov. 2020, pp. 993–998, doi: 10.1109/CAC51589.2020.9327865.

[24] M. Gregorio, F. Mandrile, and S. Musumeci, "Comparative evaluation and simulation of current control methods of LLC converters in EV battery chargers," in *2019 IEEE 5th International Forum on Research and Technology for Society and Industry (RTSI)*, Sep. 2019, pp. 188–193, doi: 10.1109/RTSI.2019.8895526.

[25] A. Mansour, M. Hajer, B. Faouzi, and G. Jamel, "Analysis and modeling of LLC resonant converter used in electric vehicle," in *2019 International Conference on Advanced Systems and Emergent Technologies (IC_ASET)*, Mar. 2019, pp. 357–362, doi: 10.1109/ASET.2019.8871008.

[26] K. Sathya and K. P. Guruswamy, "Performance analysis for LLC resonant converter in electric vehicle applications," in *2023 International Conference on Recent Trends in Electronics and Communication (ICRTEC)*, Feb. 2023, pp. 1–6, doi: 10.1109/ICRTEC56977.2023.10111915.

[27] J.-K. Han, J.-W. Kim, S.-H. Choi, J.-S. Lai, and G.-W. Moon, "Asymmetrical half-bridge converter with zero DC-offset current in transformer using new rectifier structure," in *2018 International Power Electronics Conference (IPEC-Niigata 2018 -ECCE Asia)*, May 2018, pp. 4049–4053, doi: 10.23919/IPEC.2018.8507457.

[28] D. Zhou, Y. Elasser, J. Baek, C. R. Sullivan, and M. Chen, "Inductance dual model and control of multiphase coupled inductor buck converter," in *2020 IEEE 21st Workshop on Control and Modeling for Power Electronics (COMPEL)*, Nov. 2020, pp. 1–8, doi: 10.1109/COMPEL49091.2020.9265774.

[29] A. Hendra, F. Hamada, and F. Yusivar, "Voltage control in push-pull DC-DC converter using state space averaging pid with soft-start for electric vehicle auxiliary system," in *2019 6th International Conference on Instrumentation, Control, and Automation (ICA)*, Jul. 2019, pp. 188–193, doi: 10.1109/ICA.2019.8916676.

[30] H. P. Converter, "Designing an LLC resonant half-bridge power converter designing an LLC resonant," *Power Supply Design Seminar Designing*, pp. 1–4, 2011.

[31] M. Affan, M. Noh, M. Rodhisahid, and S. Duraikannan, "Implementation of a new single-stage bridgeless boost half-bridge AC/DC converter with bidirectional switch," *Turkish Journal of Computer and Mathematics Education*, vol. 12, no. 10, pp. 1331–1341, 2021.

BIOGRAPHIES OF AUTHORS

Mohamad Affan Mohd Noh is a registered Professional Engineer in Malaysia, Senior Lecturer and the Program Leader for the B.Eng. (Hons) in Electrical and Electronic Engineering Program at the School of Engineering, Asia Pacific University of Technology and Innovation (APU), Malaysia. He holds a Ph.D. in electrical engineering and specializes in power electronics, with research interests focusing on bridgeless AC-DC converters, DC-DC converters, switched-mode power supplies (SMPS), battery chargers, energy harvesting, and modeling of power electronic circuit topologies. He can be contacted at email: mohamad.affan@apu.edu.my.

Jacques Juicy Patureau Ravina holds a Bachelor of Electrical and Electronics Engineering with honors at the Asia Pacific University of Technology & Innovation (APU), with a strong foundation in power electronics. His research contributions include the development of an LLC DC-DC resonant buck converter for electric vehicles, and his work has been recognized at the 6th International Conference on Sustainable Innovation in Engineering and Technology 2024. Notable achievements include a Silver Medal at the Malaysia Innovation Expo 2024, a Gold Award at the Hyper Interdisciplinary Conference Malaysia 2024, and Second Prize at the Innovation Design Project by IEM for the development of an Outdoor Cargo Delivery Drone. He can be contacted at email: tp062929@apu.edu.my.

Sivakumar Sivanesan is a Chartered Engineer in Malaysia, the United Kingdom, and Australia, with over 15 years of experience in academia. He began his career in one of the world's largest cathode ray tube (CRT) manufacturing companies before pursuing a Ph.D. in Engineering. His background combines strong industrial experience with a passion for education. He has led engineering programs to gain international recognition and is known for his practical, student-focused teaching approach. His work emphasizes the development of technical skills, emotional intelligence, and creativity in engineering education. His research interests include zirconia, engineering education, and nanomaterials. He can be contacted at email: siva.kumar@apu.edu.my.

Hafizul Azizi Ismail is a senior lecturer at the School of Engineering, Asia Pacific University of Technology & Innovation, Malaysia. He holds a Ph.D. in engineering from Cardiff University, United Kingdom, where his research focused on intelligent control of non-linear, underactuated electromechanical systems. His academic background includes a Master's degree in mechatronics and automatic control from Universiti Teknologi Malaysia and a Bachelor's degree in mechatronics engineering from the International Islamic University Malaysia. His research interests lie at the intersection of electrical engineering and intelligent systems, including control systems, robotics, power electronics, artificial intelligence, and energy-efficient technologies. He is a registered professional engineer with the Board of Engineers Malaysia and a Registered Energy Manager accredited by the Malaysian Energy Commission. He can be contacted at email: hafizul.azizi@apu.edu.my.

Ali Akbar Firoozi holds a Ph.D. in civil and structural engineering from Universiti Kebangsaan Malaysia (UKM). His research focuses on using nanomaterials such as nano-magnesium, nano-alumina, nano-copper, and nano-clay to stabilize clayey soils like kaolinite and illite. He developed a new mixing method for incorporating nanomaterials into soil and is skilled in various analytical techniques including XRD, XRF, NMR, FTIR, FESEM, and EDX. He has lectured at several universities and has published over 70 research papers and two books. With more than 18 years of experience in civil engineering, he has worked on over 100 projects as a designer and project manager. He can be contacted at email: firoozia@ub.ac.bw.